The following publication Pengcheng Zhao, Hoi Lut Ho, Wei Jin, Shangchun Fan, Shoufei Gao, and Yingying Wang, "Hollow-core fiber photothermal methane sensor with temperature compensation," Opt. Lett. 46, 2762-2765 (2021) is available at https://doi.org/10.1364/OL.426812.

Hollow-core fiber photothermal methane sensor with temperature compensation

PENGCHENG ZHAO[1,2,3], **HOI LUT HO**[2,3], **WEI JIN**[2,3,6], **SHANGCHUN FAN**[1,4,7], **SHOUFEI GAO**[2], **AND YINGYING WANG**[5]

[1] *School of Instrumentation and Optoelectronic Engineering, Beihang University, Beijing, China.*
[2] *Department of Electrical Engineering and Photonics Research Center, The Hong Kong Polytechnic University, Hong Kong, China.*
[3] *Photonics Research Center, The Hong Kong Polytechnic University Shenzhen Research Institute, Shenzhen, China.*
[4] *Beijing Advanced Innovation Center for Big Data-Based Precision Medicine, Beihang University, Beijing, China.*
[5] *Institue of Photonics Technology, Jinan University, Guangzhou, China*
[6] *eewjin@polyu.edu.hk*
[7] *shangcfan@buaa.edu.cn*

We demonstrate a high sensitivity all-fiber spectroscopic methane sensor based on photothermal interferometry. With a 2.4-m-long anti-resonant hollow-core fiber, a 1654 nm distributed feedback laser and a Raman fiber amplifier, a noise-equivalent-concentration of ~4.3 ppb methane is achieved at the room temperature and pressure of ~1 bar. The effects of temperature on the photothermal phase modulation as well as the stability of the interferometer are studied. By introducing a temperature-dependent compensation factor and stabilizing the interferometer at quadrature, signal instability of ~2.1% is demonstrated for temperature variation from 296 to 373 K.

Methane (CH_4) is one of the most important gases on earth, and widely used in industries, hospitals, and research laboratories [1–3]. It is a greenhouse gas and poses serious environmental and health hazards, sensitive and reliable detection of CH_4 is therefore essential for assuring civilian and industrial safety.

Tunable diode laser absorption spectroscopy (TDLAS), which measures the transmitted spectral intensity of light through an absorption cell, is a highly selective technique for gas detection. With a multi-pass or resonant cavity gas cell to increase the effective optical pathlength, and wavelength/intensity modulation and harmonic detection to reduce noise, TDLAS has demonstrated high sensitivity for detecting a wide range of absorbing gases [4, 5]. However, the gas cells used are typically made of discrete optical elements, which are bulky in size and complex to align during construction. The use of hollow-core fiber (HCF) as gas cells could reduce the complexity of optical alignment and achieve long optical pathlength with compact size. With meters-long HCF gas cells, CH_4 detection with ppm (parts-per-million) to ppb (parts-per-billion) level noise-equivalent-concentration (NEC) have been demonstrated in the near-infrared (NIR) [6] and mid-infrared (MIR) [7–9], respectively.

Photothermal (PT) spectroscopy is a derivative of laser absorption spectroscopy and it detects the refractive index (RI) change of the gas medium due to absorption of a pump beam [10]. CH_4 detection with PT deflection spectroscopy was demonstrated by Y. Li et al [11] and further developed with cantilever-enhanced structure for sensitive detection [12]. The PT deflection spectroscopy relies on detecting the deflection of a probe laser beam by a position-sensing detector, which is insufficient for high sensitivity applications. Recently, PT interferometry (PTI) spectroscopy with HCF gas cells has been demonstrated[13]. PTI uses a pump-probe approach: gas absorption of a modulated pump results in periodic heat generation, which modulates the phase of a probe beam. The probe phase modulation is proportional to the length of the gas cell and the pump power in the HCF, and enhanced sensitivity can be achieved by use of a higher power pump laser. With distributed feedback (DFB) lasers in the NIR and erbium-doped fiber amplifier (EDFA) to amplify the pump power to a hundred milliwatt-level, detections of acetylene down to ppb to ppt (parts-per-trillion) NEC have been demonstrated [13–17]. However, the absorption lines of CH_4 in the NIR are not as strong as acetylene and are not in wavelength range of EDFAs, which hinders the development of CH_4 sensors with high sensitivity.

In this paper, we demonstrate ppb-level CH_4 detection with all-fiber PTI by use of a Raman amplified 1654-nm DFB pump laser and a stabilized 1550-nm dual-mode probe interferometer. We study, for the first time to our knowledge, the effects of temperature change on the probe phase modulation and detection. With a simple temperature compensation scheme, signal fluctuation as small as

~2.1% is demonstrated over a temperature range from 296 K (room temperature) to 373 K (100 °C).

Fig. 1(a) shows the experimental setup. We choose to operate the pump at the R(3) absorption line of 2v3 band of CH_4 at ~1653.72 nm (6046.96cm^{-1}), which is within the transmission window of standard single mode fibers (SMFs) and where spectral crosstalk with water vapor (H_2O) and carbon dioxide (CO_2) could be negligible, as shown in Fig. 1(b). The pump from a 1654-nm DFB is amplified by a Raman amplifier with maximum output power of ~220 mW. The Raman amplifier is backward pumped, which includes a Er-doped fiber ASE source with a passband of ~10 nm and an EDFA that give maximum output power of ~9 W, an ~0.8-km-long OFS Raman fiber with Raman gain efficiency of 2.5 (W·km)$^{-1}$, and two wavelength-division multiplexers (WDM1 and WDM2). The wavelength of the DFB is scanned slowly across the R(3) absorption line via thermal tuning and at the same time sinusoidally current-modulated at a higher frequency to generate periodic PT phase modulation. The gas cell is made of a 2.4-m-long anti-resonant HCF (AR-HCF) looped to a diameter of ~40 cm. The HCF has a hollow-core of ~30 µm in diameter, inscribed by a single ring of seven silica capillaries with diameter of ~14 μm and thickness of ~370 nm, and the cross-section of the HCF is shown in inset of Fig. 1(a). The attenuations for the fundamental mode of the AR-HCF are 0.18 and 0.25 dB/m at the wavelengths of the probe (~1550 nm) and the pump (~1654 nm), respectively. The probe is from a single frequency 1550 nm fiber laser equipped with a piezo-electric wavelength tuning mechanism.

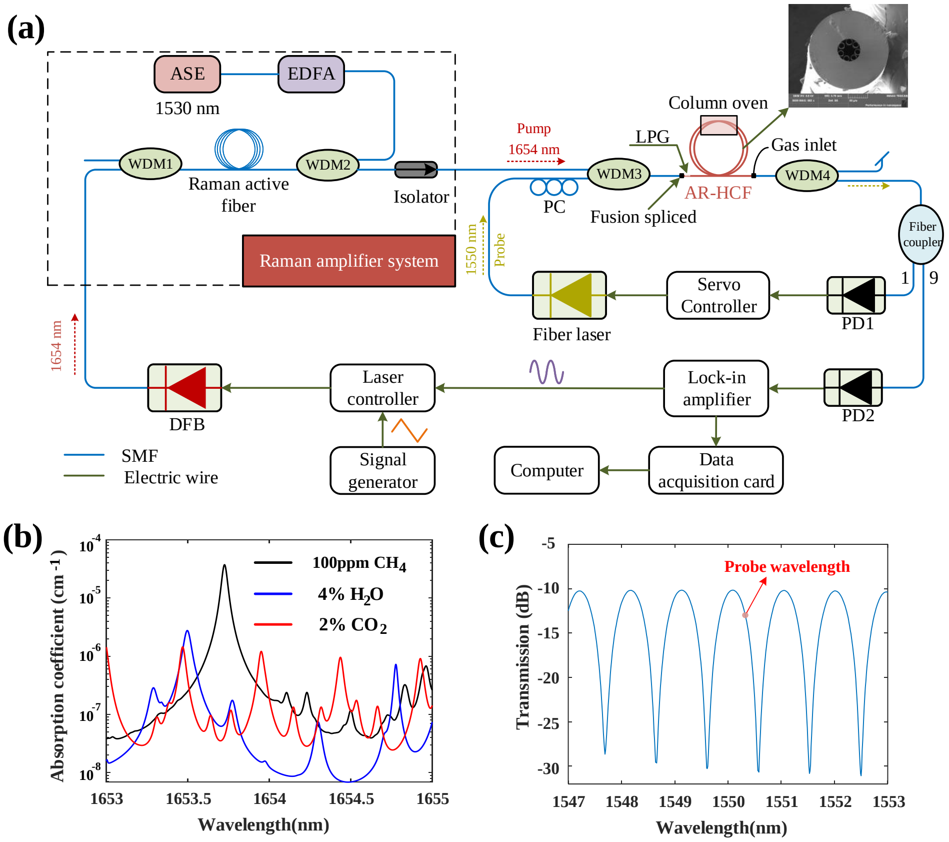

Fig. 1. (a) Experimental setup for gas detection with a 2.4-m-long AR-HCF. ASE, amplified spontaneous emission source; EDFA, erbium-doped fiber amplifier; DFB, distributed feedback laser; WDM1-WDM4, wavelength-division multiplexers; PC, polarization controller; LPG, long period grating; PD1-PD2, photodetectors. (b) Calculated absorption spectra of 100 ppm CH_4, 4% H_2O and 2% CO_2 based on HITRAN database[18]. (c) Transmission spectrum of the SMF-LPG-HCF-SMF modal interferometer.

The probe and pump are combined by WDM3 and delivered to the AR-HCF gas cell. The SMF pigtail of WDM3 is fusion spliced to the AR-HCF to excite primarily the fundamental LP_{01} mode in the AR-HCF. To detect the PT phase modulation, we use a dual-mode interferometer similar to that described in [19]. A long period grating (LPG) is inscribed on the AR-HCF just after the input splice by a pulsed CO_2 laser to couple a fraction of the probe power from the LP_{01} to LP_{11} mode. The LPG has 29 grating periods and a grating pitch of ~1.52 mm, which resonantly couples ~50% of light power from LP_{01} mode to LP_{11} mode for the probe but not the pump. The total loss of the pump is measured to be ~2.6 dB, including ~0.3 dB by the LPG. The SMF-HCF splice joint and the LPG are well fixed on a base for protection. The output end of the AR-HCF is offset aligned and mechanically connected to an output SMF, with an air-gap of ~2 μm between them for gas filling. The SMF-LPG-HCF-SMF structure forms a dual-mode interferometer, which is used to detect the differential phase modulation between the two probe modes (i.e., LP_{01} and LP_{11}) due to pump absorption of the gas molecules. Fig. 1(c) shows the transmission spectrum of the modal interferometer, which is measured with a broadband source and an optical spectrum analyzer with wavelength resolution of 50 pm. The free spectral range and contrast of the interference fringes are ~1 nm and ~20 dB, respectively.

Gas filling is carried out by firstly pressurizing the calibrated 107 ppm CH_4 balanced by nitrogen (N_2) into the pre-vacuum AR-HCF gas cell from the gas inlet. The gas pressure is then released to the ambient pressure, and the gas valve is closed to maintain constant pressure in the HCF. After about half an hour, we start to conduct gas detection experiment, and the system is stable over many hours. The optimal frequency and root-mean-squared voltage of the pump modulation, corresponding to maximum signal-to-noise ratio for the PT phase detection, are determined to be 6 kHz and 130 mV, respectively. The optimal modulation voltage corresponds to a wavelength modulation depth m of 2.2 times the R(3) absorption linewidth of CH_4, where $2f$ signal is maximized [20]. All the gas experiments were then conducted under these optimal settings.

Fig. 2(a) shows the $2f$ lock-in output (PT signal) when the pump wavelength was tuned across the R(3) absorption line of CH_4 with different pump power levels. Fig. 2(b) shows the peak-to-peak value of PT signal and standard deviation (s.d.) of noise as functions of pump power levels, where the s.d of noise was determined based on recorded 2-minute $2f$ lock-in output for 1 s lock-in time constant with pump wavelength tuned away from absorption line to ~1654.00 nm. With pump power of ~118 mW in the HCF, the NEC is calculated to be ~8.7 ppb, giving a noise equivalent absorption (NEA) of ~3.2×10^{-9}cm^{-1}.

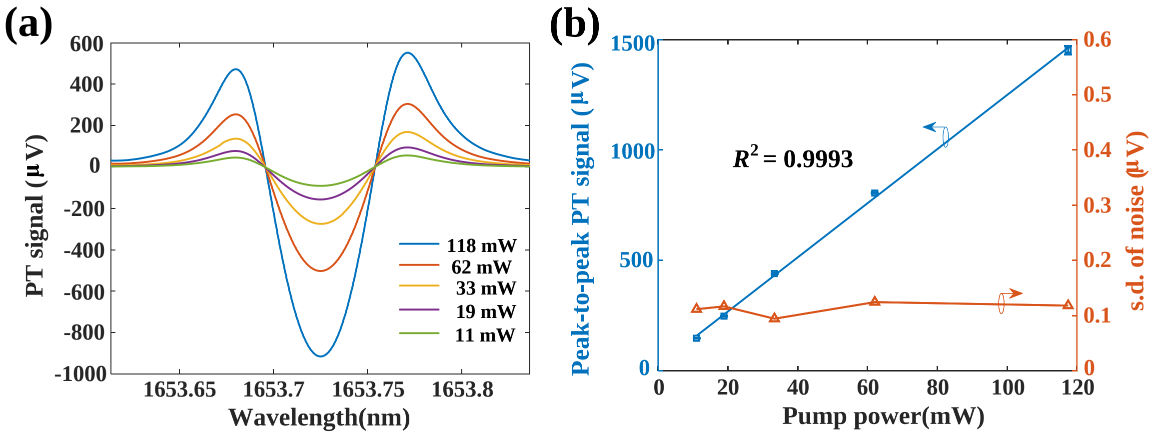

Fig. 2. (a) The PT signal with pump wavelength tuned across the R(3) absorption line of CH_4. (b) The peak-to-peak value of the PT signal and the s.d. of noise as functions of input pump power levels. Error bars show the s. d. from five measurements. The mean probe power on the PD2 is -3.7 dBm. The lock-in time constant of 1 s and filter slope is 18 dB Oct $^{-1}$, corresponding to 0.094 Hz detection bandwidth.

Allan-Werle deviation plots for two different experimental conditions, i.e., the pump laser is on (black dots) and off (red dots), are presented in Fig. 3. When the pump is off, the random noise has a $\tau^{-1/2}$ dependence on the integration time τ, mainly due to the relative intensity noise of the probe. At short time scales, the Allan deviation for pump-on is close to the results for pump-off. The NEC goes down to ~4.3 ppb (NEA of ~1.6×10^{-9} cm^{-1}) with 100 s integration time. However, increasing the integration time does not lead to further improvement of the detection limit, which is limited by the pump power fluctuations.

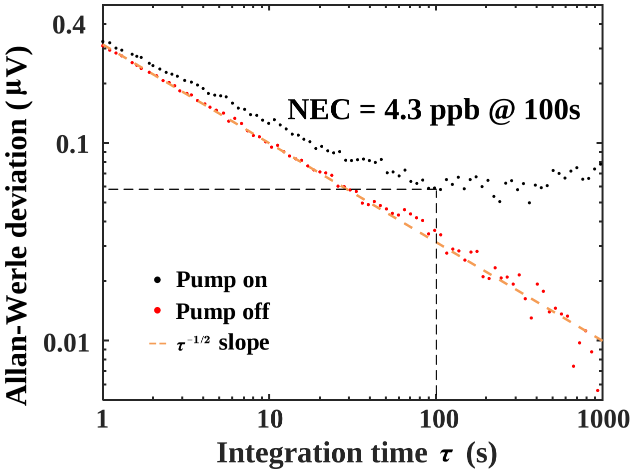

Fig. 3. Allan-Werle deviation plots based on noise data over a period of 2 hours with pump laser on and off respectively. The lock-in time constant is 30 ms, corresponding to 3.125 Hz detection bandwidth.

The effects of temperature on the PT phase modulation as well as the stability of the dual-mode interferometer are studied. Based on the theoretical analyses in previous work [11, 16, 17], at the limit of low pump modulation frequency, the PT phase modulation for a particular mode i (i.e., LP_{01} or LP_{11}) in HCF may be expressed as

$$\phi_i = \frac{2\pi}{\lambda} \cdot \frac{\mathrm{d}n}{\mathrm{d}T} \frac{\chi_i H_{2f} P_p C \alpha_{v_0}}{\kappa} \cdot L \tag{1}$$

where λ (nm) is the probe wavelength, P_p (mW) is the pump power level, C is the target gas ($\mathrm{CH_4}$) concentration, and L is the length of the HCF. χ_i is a constant related to HCF structure and probe mode field, which has a different value for the probe LP_{01} and LP_{11} modes. By using Equ.(1), the differential PT phase modulation $\Delta\phi = \phi_{\mathrm{LP}_{01}} - \phi_{\mathrm{LP}_{11}}$ can be calculated. Other parameters, which are relatively strongly affected by temperature, are listed in Table 1.

Similar to TDLAS, the scale factor ($\mathrm{d}\phi_i/\mathrm{d}C$) of the PT phase modulation is affected by the temperature-dependent absorption coefficient α_{v_0} [21] and the absorption linewidth γ that determines the amplitude of the $2f$ coefficient H_{2f}. In addition, the scale factor is also affected by the temperature-dependence of thermo-optic coefficient $\mathrm{d}n/\mathrm{d}T$ and thermal conductivity κ of balance gas, as shown in Table 1. By using Equ.(1), for a temperature rise from 296 to 373 K, the fractional changes of PT phase modulation due to contribution of $\mathrm{d}n/\mathrm{d}T$, κ, α_{v_0} and H_{2f} are respectively ~63%, 83%, 72% and 98%, respectively, as shown in the far-right column of Table 1.

Table 1. Temperature dependent parameter $X(T)$ and the corresponding change of PT phase modulation ϕ_i for temperature (T) variation from 296 to 373 K at 1 bar

Variable X	Expression $X(T)$	$\frac{\phi_i(X(373\mathrm{K}))}{\phi_i(X(296\mathrm{K}))}$
Thermo-optic coefficient of $\mathrm{N_2}$ $\mathrm{d}n/\mathrm{d}T$ ($\mathrm{K^{-1}}$) [22]	$-\frac{\mu P}{T^2}$	~63%
Thermal conductivity of $\mathrm{N_2}$ κ ($\mathrm{mW\ m^{-1}\ K^{-1}}$) [23]	$\sqrt{T}\left(-92.39\frac{1}{T} + 1.647 + 5.255 \times 10^{-4} T\right)$	~83%
Absorption coefficient of R(3) line of $\mathrm{CH_4}$ $\alpha_{v_0}(\mathrm{cm^{-1}})$ [21]	$\frac{1}{\pi\gamma(T)} \cdot P S_{v_0}(T_{\mathrm{ref}}) \frac{T_{\mathrm{ref}}}{T} \frac{Q(T_{\mathrm{ref}})}{Q(T)} \cdot \left[\frac{1-e^{-\frac{v_0}{k_B T}}}{1-e^{-\frac{v_0}{k_B T_{\mathrm{ref}}}}}\right] e^{-\frac{E''}{k_B}\left(\frac{1}{T}-\frac{1}{T_{\mathrm{ref}}}\right)}$	~72%
$2f$ coefficient H_2	$\frac{2}{m^2}\left[\frac{m^2+2}{\sqrt{m^2+1}} - 2\right]\Bigg\vert_{m=2.2\frac{\gamma(T_{\mathrm{ref}})}{\gamma(T)}}$	~98%

Note: μ = 0.082 ($\mathrm{K{\cdot}atm^{-1}}$) is a constant, P (atm) is the pressure, T_{ref} = 296 K is the reference temperature, $\gamma(T) = P\,(T_{\mathrm{ref}}/T)^{0.817}\,\gamma(T_{\mathrm{ref}})$ ($\mathrm{cm^{-1}}$) and S_{v_0} ($\mathrm{cm^{-2}{\cdot}atm^{-1}}$) are HWHM linewidth [24] and line strength at v_0 = 6046.96 ($\mathrm{cm^{-1}}$) of methane respectively, $Q(T) = (T/T_{\mathrm{ref}})^{3/2} Q(T_{\mathrm{ref}})$ is the internal partition function, E'' = 62.8782 ($\mathrm{cm^{-1}}$) is the low-state energy of the transition, k_B = 0.695 ($\mathrm{cm^{-1}{\cdot}K^{-1}}$) is the Boltzmann constant. The $2f$ signal is maximized when wavelength modulation depth m = 2.2 [20].

Furthermore, temperature variation also affects the probe interferometer, which would cause drift of the operating point from the quadrature operation and hence result in a change on the conversion efficiency of phase-to-intensity modulation. This could however be overcome by servo tuning the probe wavelength to a quadrature of interference fringe.

The effects of temperature variation on gas detection were studied experimentally by placing two sections of AR-HCF (~47 cm out of 2.4 m) inside a column oven and applying a temperature excursion over a period of 2.5 hours. The pump wavelength is tuned to the center of the R(3) absorption line of $\mathrm{CH_4}$ while the temperature in the oven was changed from 296 to 373 K with two intermediate stages (i.e., 323 K, 348 K) in the first half an hour and then allowed to dissipate heat through natural cooling. In the first experiment, the servo-loop was open, and we manually tuned the probe wavelength to a quadrature of the interference fringe before applying the temperature change and recorded the DC component from PD1 during the temperature excursion. The variation of the operating phase (orange line) converted from DC intensity change of the probe and the applied temperature (yellow line) with time are shown in left panel of Fig. 4(a). As is seen, the operating point of the interferometer is highly sensitive to temperature and deviates as much as 7° from the quadrature operation at 373 K. To minimize PT signal degradation due to change of the operating point, we closed the servo-loop to lock the probe wavelength to a quadrature of interference fringe and conducted the gas detection experiments. The working point of interferometer (blue line) is well locked to quadrature during the entire experimental period of 2.5 hours, as shown in the right panel of Fig. 4(a). Fig. 4(b) shows the $2f$ lock-in output for 107 ppm $\mathrm{CH_4}$ in $\mathrm{N_2}$ during the applied temperature excursion. The $2f$ signal (orange dots) reduces as much as 9.4% at 373 K, which is close to the theoretical estimations of 12.3% from Equ.(1) by taking the factor of heated fiber length (47 cm out of 2.4-m HCF) into account. The discrepancy may be due to temperature-dependent pressure change inside the HCF, which was not considered in our theoretical calculation. Based on the measured results, the PT signal and temperature relationship can be fitted to a linear relationship. By using this relation to perform temperature compensation, the PT signal fluctuation reduces down to ~2.1% (blue dots) over the entire temperature excursion. For comparison, we also plot the signal variations in ambient lab environment when the servo-loop is on (stabilized at quadrature) and off (free running, un-stabilized), as shown in Fig. 4(c). The maximum signal fluctuations are respectively 1.9% and 2.5% over a period of 6 hours.

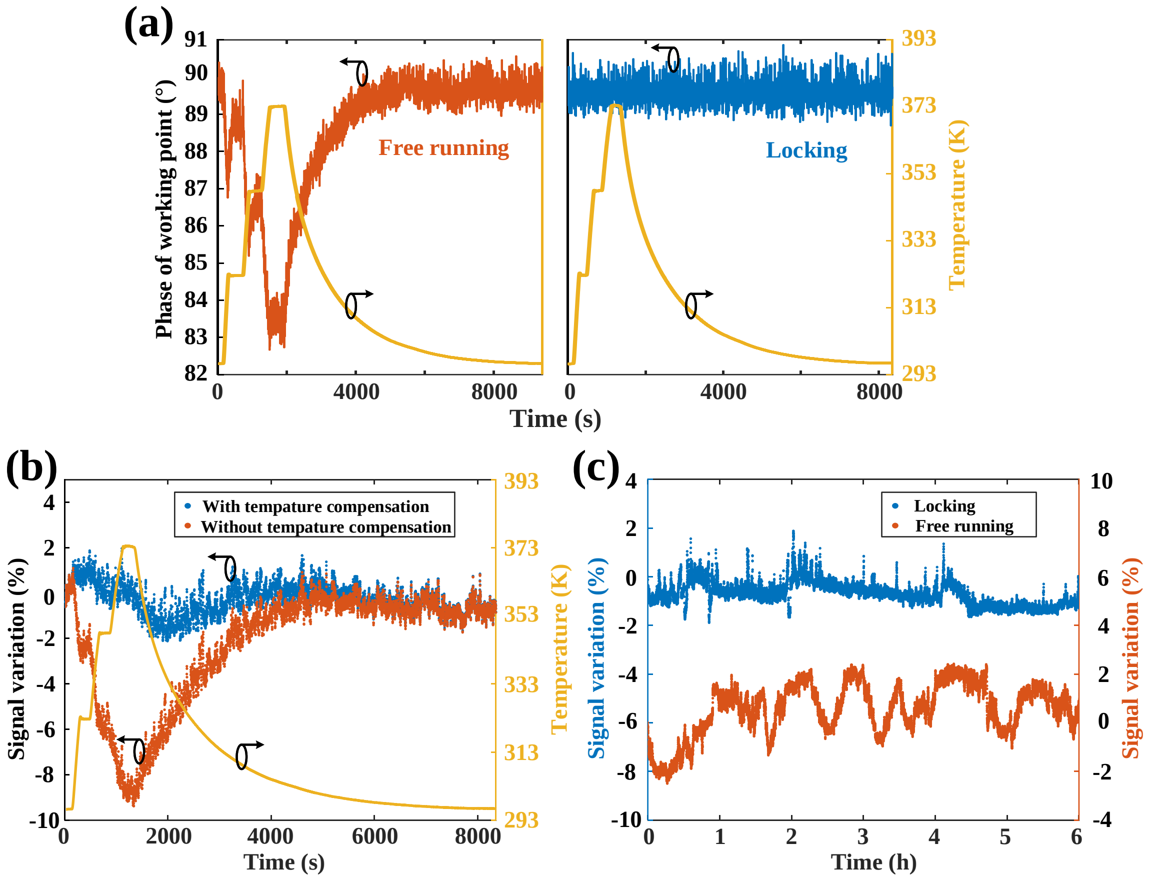

Fig. 4. (a) The operating phase of interferometric detection system without (left panel) and with (right panel) locking the probe wavelength to quadrature. (b) $2f$ signal variations without and with temperature compensation when the probe interferometer is stabilized at quadrature. (c) Long-term stability of the gas detection system in laboratory environment when the probe interferometer is stabilized at quadrature (blue dots) and free running (orange dots), respectively. The sampling frequency is one sample per second.

Table 2 summarizes the performance of several recently reported HCF-based CH_4 gas sensors. The MIR CH_4 sensors offer considerably lower detection limit than the NIR sensors using conventional absorption spectroscopy due to stronger absorption line strength. Here, we use NEA, independent of absorption line strength, to compare the performance of gas sensors. The performance of the NIR PTI sensor we demonstrated here is about four times better in terms of NEC or nearly two orders of magnitude better in NEA than the state-of-the-art MIR HCF-based CH_4 sensor [8].

In summary, we have reported a high sensitivity all-fiber PTI spectroscopic CH_4 sensor. With a 2.4-m-long AR-HCF gas cell and a Raman amplifier, we demonstrated CH_4 detection with ~4.3 ppb for 100 s integration time at room temperature and pressure of ~1 bar, the lowest one among all the reported HCF-based CH_4 sensors so far to our knowledge. We studied the effects of temperature change on PT phase modulation and found that the temperature-dependent thermo-optic coefficient and thermal conductivity of balance gas as well as the absorption strength and linewidth of target gas (CH_4) significantly affect the PT phase modulation. Temperature test of the gas detection system over the range of room temperature to 373 K demonstrated PT signal variation of ~9.4%, which can be reduced to ~2.1% by using a simple linear temperature compensation scheme.

Funding. Hong Kong SAR government (GRF 15260316), National Natural Science Foundation of China (61827820, 61675011), the Local Innovative and Research Teams Project of Guangdong Pear River Talents Program (Grant No. 2019BT02X105), and the Hong Kong Polytechnic University (Grant Nos. P0034330 and 1-9B65), the Program for Changjiang Scholars and Innovative Research Team in University (grant-IRT_16R02).

Disclosures. The authors declare no conflicts of interest.

Data availability. Data underlying the results presented in this paper are not publicly available at this time but may be obtained from the authors upon reasonable request.

Table 2. Performance comparison of recently reported HCF-based CH_4 sensors

Year	Method / Fiber	Integration time	NEC	NEA/cm^{-1}
2017 [25]	WMS / 0.8 m HC-PBF	10 s	1.4 ppm	5.22×10^{-7}
2018 [26]	WMS / 1.3 m Kagome	Not stated	4.1 ppm	3.16×10^{-5}
2019 [6]	WMS / 0.45 m HC-PBF	75 s	360 ppb	1.34×10^{-7}
2019 [7]	DS / 1.3 m Kagome	100 s	65 ppb	5.01×10^{-7}
2019 [8]	DAS / 1 m HCF	Not stated	17 ppb	1.31×10^{-7}
2020 [9]	WMS / 1 m AR-HCF	40 s	24 ppb	1.85×10^{-7}
This work	PTI / 2.4m AR-HCF	100 s	4.3 ppb	1.60×10^{-9}

WMS, wavelength modulation spectroscopy; DS, dispersion spectroscopy; DAS, direct absorption spectroscopy; The NEA data were calculated from NEC data and the absorption line strength in HITRAN database [18].

REFERENCES

1. J. R. Rostrup-Nielsen, Catal. today **18**, 305 (1993).
2. S.-Y. Lee and G. D. Holder, Fuel Process. Technol. **71**, 181 (2001).
3. B. de Lacy Costello, M. Ledochowski, and N. M. Ratcliffe, J. breath research **7**, 024001 (2013).
4. X. Liu, S. Cheng, H. Liu, S. Hu, D. Zhang, and H. Ning, Sensors **12**, 9635 (2012).
5. J. Hodgkinson and R. P. Tatam, Meas. Sci. Technol. **24**, 012004 (2012).
6. L. Hu, C. Zheng, D. Yao, D. Yu, Z. Liu, J. Zheng, Y. Wang, and F. K. Tittel, Infrared Phys. & Technol. **97**, 101 (2019).
7. K. Krzempek, K. Abramski, and M. Nikodem, Sensors **19**, 3352 (2019).
8. S. Huang, Y. Huang, and H. Chui, Sensors Actuators B: Chem. **282**, 599 (2019).
9. P. Jaworski, P. Kozioł, K. Krzempek, D. Wu, F. Yu, P. Bojęś, G. Dudzik, M. Liao, K. Abramski, and J. Knight, Sensors **20**, 3813 (2020).
10. S. E. Bialkowski, *Photothermal spectroscopy methods for chemical analysis*, vol. 177 (John Wiley & Sons, 1996).
11. Y. Li and R. Gupta, Appl. Opt. **42**, 4396 (2003).
12. M. Rahimi, I. Chae, J. E. Hawk, S. K. Mitra, and T. Thundat, Sensors Actuators B: Chem. **221**, 564 (2015).
13. W. Jin, Y. Cao, F. Yang, and H. L. Ho, Nat. Commun. **6**, 1 (2015).
14. Y. Lin, W. Jin, F. Yang, Y. Tan, and H. L. Ho, Opt. Lett. **42**, 4712 (2017).
15. F. Yang, Y. Tan, W. Jin, Y. Lin, Y. Qi, and H. L. Ho, Opt. Lett. **41**, 3025 (2016).
16. H. Bao, Y. Hong, W. Jin, H. L. Ho, C. Wang, S. Gao, Y. Wang, and P. Wang, Opt. Express **28**, 5423 (2020).
17. P. Zhao, Y. Zhao, H. Bao, H. L. Ho, W. Jin, S. Fan, S. Gao, Y. Wang, and P. Wang, Nat. Commun. **11**, 1 (2020).
18. I. E. Gordon, L. S. Rothman, C. Hill, R. V. Kochanov, Y. Tan, P. F. Bernath, M. Birk, V. Boudon, A. Campargue, K. Chance *et al.*, J. Quant. Spectrosc. Radiat. Transf. **203**, 3 (2017).
19. P. Zhao, H. L. Ho, W. Jin, S. Fan, S. Gao, Y. Wang, and P. Wang, Opt. Lett. **45**, 5660 (2020).
20. J. Reid and D. Labrie, Appl. Phys. B **26**, 203 (1981).
21. J. Cao, K. Zhang, Z. Wang, R. Yang, and Y. Wang, 2010 Symp. on Photonics Optoelectronics pp. 1–5 (2010).
22. Y. Clergent, C. Durou, and M. Laurens, J. Chem. & Eng. Data **44**, 197 (1999).
23. T. Hoshino, K. Mito, A. Nagashima, and M. Miyata, Int. J. Thermophys. **7**, 647 (1986).
24. M. Gharavi and S. G. Buckley, J. Mol. Spectrosc. **229**, 78 (2005).
25. Q. He, P. Dang, Z. Liu, C. Zheng, and Y. Wang, Opt. Quantum Electron. **49**, 115 (2017).
26. M. Nikodem, K. Krzempek, G. Dudzik, and K. Abramski, Opt. Express **26**, 21843 (2018).